Geomech. Geophys. Geo-energ. Geo-resour. (2024) 10:80
https://doi.org/10.1007/s40948-024-00791-9

RESEARCH

Sol–gel-stabilized CO_2 foam for enhanced in-situ carbonation in foamed fly ash backfill materials

Ichhuy Ngo · Liqiang Ma · Zhiyang Zhao · Jiangtao Zhai · Kunpeng Yu · Yonghui Wu

Received: 27 June 2023 / Accepted: 2 April 2024

Abstract A novel highly stable aqueous foam was synthesized using CO_2, sodium silicate (SS) and anionic surfactant of sodium dodecylbenzene sulfonate. The influence of CO_2 foam on the mechanical properties and its underlying mechanisms of foamed backfill material was investigated. The experimental results revealed that the addition of CO_2 and SS effectively reduced the drainage of the foam while strengthening the liquid film of the Plateau borders, which stabilizes the foam. The excellent stability is attributable to the gel network developed after SS exposed to CO_2, that adhere to the foam surface. Furthermore, due to the interaction between encapsulated CO_2 and hydration products, micro $CaCO_3$ formed and filled the pore wall; thus, precast foam forms robust pore structures in the hardened foamed backfill.

I. Ngo (✉) · L. Ma (✉) · Z. Zhao · J. Zhai · K. Yu · Y. Wu
School of Mines, China University of Mining and Technology, Xuzhou 221116, China
e-mail: ngoichhuy@cumt.edu.cn

L. Ma
e-mail: ckma@cumt.edu.cn

I. Ngo
Key Laboratory of Xinjiang Coal Resources Green Mining (Xinjiang Institute of Engineering), Ministry of Education, Urumqi 830023, China

Article highlights

- A novel highly stable CO_2 foam was formulated using the sol-gel method.
- The stability and foaming mechanisms of CO_2 foam were investigated.
- The performances of foamed fly ash backfill materials were characterized.

Keywords CO_2 foam · Sol–gel reaction · Carbonation · Fly ash · Foamed backfill material · CO_2 utilization

Abbreviations

SS	Sodium silicate
SDBS	Sodium dodecylbenzene sulfonate
CFB	CO_2 foamed backfill material
UCS	Uniaxial compressive strength
SEM	Scanning electron microscopy
EDS	Energy dispersive spectroscopy
XRD	X-ray diffraction
XRF	X-ray fluorescence
C_2S	Dicalcium silicate
C_3S	Tricalcium silicate
L/S	Liquid to solid ratio
TG	Thermogravimetric analysis
CH	Calcium hydroxide
C-A-S-H	Calcium aluminosilicate hydrate

Published online: 29 April 2024

1 Introduction

China's coal and electricity integration strategy has optimized to reduce coal resource production and consumption, that is to achieve the carbon neutrality. However, the challenge has yet to be overcome, as a large amount of CO_2 is emitted during the operation of a coal-fired power plant (Guo et al. 2023a; Zhang et al. 2023a). On average, approximately 2.4 tons of CO_2 is produced by 1 ton of coal combustion, together with up to 0.1 ton of fly ash (Asghar et al. 2021). The determination of an effective means to sequester and utilize CO_2 has become one of the most vital topics of research for many scholars, especially with a combination of fly ash. Currently, CO_2 sequestration and utilization in coal power plants are based primarily on the preparation of costly chemical additives, biological utilization, mineralization utilization, and enhanced oil and gas recovery (Zhi et al. 2023; Bakonyi, et al. 2020; Ostovari, et al. 2023; Ngo et al. 2020; Power et al. 2021; Yadav and Mehra 2021; Pan et al. 2018; Zhang et al. 2023b). Scholars also proposed the hydrate-based CO_2 sequestration, where in-situ minerals and chemical additives were considered their effects on nucleation and growth kinetics of CO_2 hydrate (Ren et al. 2023; Liu et al. 2022).

Nevertheless, the aforementioned methods present economic viability disadvantages owing to long transportation and high sequestration costs. In this regard, many scholars have researched CO_2 sequestration in fly ash by carbonation means to serve as a bridge connecting CO_2 sequestration from a coal-fired power plant and functional materials for mining. Li et al. (2023) carried out direct aqueous carbonation in industrial/mining solid waste, where the CO_2 sequestration is 540 g-CO_2/kg by applying a carbonation temperature of 60 °C. With identical carbonation temperature, Miao et al. (2023) addressed that the maximum CO_2 sequestration in circulating fluidized bed combustion fly ash was 128 g-CO_2/kg. Wu et al. (2022) studied the effect of high temperature CO_2 (20–140 °C) on carbonation performance of recycled concrete fines, and found that the optimal temperature is 100 °C with a CO_2 uptake of 12.65%. Miao et al. (2020) carried out an aqueous CO_2-cement interaction experiment and investigated its characteristics at pre- and post-exposure using X-ray computed micro-tomography. Their finding has lightened up the CO_2 sequestration and utilization in mine solid waste materials, but the current method shares the same issue, where slurry preparation time is extended owing to the long aqueous carbonation process. As addressed in our previous study (Ngo et al. 2023a), a high strength CO_2 carbonated backfill material with a carbonation capacity of 1390 g-CO_2/kg-backfill materials was successfully prepared with a high fly ash content. However, the backfill slurry required long mechanical stirring and CO_2 aqueous carbonation during preparation. This was thought to affect the working efficiency in the field implementation. To respond, CO_2 foamed backfill material (CFB) is proposed, so that the carbonation by CO_2 foam could go simultaneously during filling and after standing in mine goaf.

Currently, the research on the preparation and characteristics of CFB is limited. Guan et al. (2023) prepared foam concrete from a synthetic foaming agent of animal protein and vegetable oil, ordinary Portland cement P.O. 42.5, soil and fly ash, where the resulted UCS was 4–0.28 MPa at the target density of 800–1200 kg/m^3. Zhang et al. (2020) prepared foamed concrete with a density of 600–800 kg/m^3 and UCS of 0.4–3.6 MPa by mixing ordinary Portland cement P.O. 42.5, silt and foaming agent. Chen et al. (2021) prepared foam concrete from ordinary Portland cement, fly ash and foaming agent of an albescent, where the UCS was 1–5.2 MPa at a density of 500–1000 kg/m^3. Yang et al. (2021) prepared foam concrete with a density of 292–686 kg/m^3 and a UCS of 0.4–5.5 MPa by mixing gypsum, red mud, aluminum ash, carbide slag, limestone tailings, gold tailing, animal protein foaming agent, hydroxypropyl methylcellulose, polycarboxylate superplasticizer. Xiao et al. (2022) prepared foam concrete from ordinary Portland cement, sulfonaluminate cement, recycled powder and compound foaming agent, where the density was 557–584 kg/m^3 and the UCS was 0.75–2.05 MPa. From the perspective of the foaming method, physical foaming not only features higher foaming efficiency and uniform and controllable bubble sizes, but can also directly capture CO_2 within the foam bubble compared to chemical foaming.

Owing to the poor stability of CO_2 foam and its characteristics of easy chemical reaction with cementitious materials (Wang et al. 2023; Liu et al. 2023), the foaming effects of CFB by CO_2 were not obvious. This resulted in the fact that the method of preparation of CFB is still unclear. In fact, there may be no

research report on the successful preparation of CFB using CO_2 foam and the evaluation of its basic performance and carbon sequestration potential. In our previous researches (Ngo et al. 2022; 2023b), a development of silica gel was observed by a reaction between CO_2 and sodium silicate (SS) during backfill slurry and grouting solution preparation. In this regard, inclusion of a silicate additive in the foaming agent is expected to improve the foam stability and foam pore structure of CFB through a sol–gel reaction. Increasing the foam amount appropriately can improve the porosity and the foaming effect of foamed backfill material (Xu et al. 2023). Therefore, this work aimed to propose a sol–gel method of CO_2 foam by adding a silicate additive in the foaming agent as the precursor. To the best of our knowledge, this study has yet been investigated by other scholars. In this study, the CFB was successfully prepared using the sol–gel method in CO_2 foam. The compressive strength test, thermogravimetric analysis, scanning electron microscopy (SEM), energy dispersive spectroscopy (EDS), and X-ray diffraction (XRD) were carried out to investigate the effects of CO_2 foam on CFB dry density, compressive strength, pore structure, and carbon sequestration. The results were crucial for a more in-depth understanding of the mechanisms of CO_2 foam in foamed backfill materials and the feasible implementation of CFB in coal mine goaf.

2 Experiments

2.1 Materials

Sodium dodecylbenzene sulfonate (SDBS) was obtained from Sinopharm Chemical Reagent Co., Ltd. (99.9% pure, Shanghai, China) and used as the foaming agent due to its interfacial active characteristic. Sodium silicate (SS) with a molecular mass of 284.22 g/mol purchased from Sigma-Aldrich Co., Ltd, 99.9% pure, used as pH modification agent in foaming solution and alkali activator in foamed backfill material slurry. All chemical reagents were analytical grade and were used as received without further fabrication. CO_2 gas was supplied by Xuzhou Luyou Gas Co., Ltd. Fly ash was acquired from a coal power plant in Zhengzhou, Henan Province, China. The fly ash sample was oven dried at 60 °C for 48 h to remove residue moisture. The Ordinary Portland cement (P.O. 42.5) was bought from Zhucheng Yangchun Co., Ltd. Their oxide and mineral composition were analyzed using X-ray fluorescence (XRF, Bruker model S8 Tiger spectrometer, Germany) and X-ray diffraction (XRD, Bruker model D8 Advance, Germany), respectively, as shown in Table 1. Fly ash possesses mainly SiO_2, Al_2O_3 and Fe_2O_3 corresponding to mullite, quartz, and hematite, where cement consists of oxide of CaO, SiO_2, Al_2O_3 and MgO corresponding to tricalcium silicate (C_3S), dicalcium silicate (C_2S), lime and periclase.

Table 1 Composition of the oxides of the raw materials

Oxides	Composition (wt%)	
	Fly ash	Cement
SiO_2	53.43	23.20
Al_2O_3	31.93	8.07
Fe_2O_3	3.36	3.16
CaO	2.08	49.95
K_2O	1.29	0.94
TiO_2	1.18	0.53
MgO	0.53	4.69
SO_3	0.53	4.12
P_2O3	0.18	0.18
Others	5.16	5.16
Minerals	Mullite, quartz and hematite	Tricalcium silicate (Ca_3SiO_5), dicalcium silicate (Ca_2SiO_4), lime (CaO), and periclase (MgO)

2.2 Sample preparation

2.2.1 *Foaming agent solution and prefabricated foams*

Table 2 presents the composition of the foaming samples, which consisted of SDBS, SS, and deionized water fabricated using ambient air and CO_2. First, SS was dissolved within deionized water to obtain an alkali solution with a pH of 8. Then 5 wt% SDBS was added to the alkali solution and stirred at room temperature for 1 h at a constant mixing speed of 500 rpm. Finally, prefabricated foam was prepared by injecting a certain proportion of compressed air or CO_2 into each of the foaming agent solutions, which was then mixed to produce foam. It should be noted that the flow rate was controlled for both air and CO_2 to ensure that a constant volume of air or CO_2 was used to prepare each foam sample.

2.2.2 *Foamed backfill specimens*

The foamed backfill specimens were produced from fly ash, cement, water, SS and prefabricated foam. The target density, fresh density, actual dry density, and mix proportions of foamed backfill were summarized in Table 3. In a conventional procedure, fly ash and cement were mixed thoroughly in the dry state to ensure dry phase homogeneity. Meanwhile, SS was dissolved in water to form an SS solution. Then the SS solution and the dry mixture were successively added to a mortar mixer, and the resulting mixture was stirred at 500 rpm for 5 min. The mixed backfill paste was treated with prefabricated air/CO_2 foam, respectively, and the resulting mixture was stirred at 500 rpm for 2 min, at which point the foam was uniformly distributed. Subsequently, the fresh foamed backfill slurry was poured into a standard cylindrical mold of Φ 50 mm × 100 mm, which was then covered with plastic film to prevent water evaporation. These foamed backfill specimens were allowed to stand at room temperature for 48 h. Then, the specimens were demolded and placed in a curing box with a constant temperature of 20 ± 2 °C and a humidity of 95 ± 2% until reaching the corresponding curing time. To investigate the effects of CO_2 foam in the backfill mixture, the volume of added foam was varied in 200, 400 and 600 mL corresponding to a density of ~ 600, 500, and 400 kg/m^3, respectively.

Table 2 Composition of prefabricated foams

Sample	SDBS (wt%)	SS (wt%)	Air/CO_2	Foam pH
Foam-air	5	0.25	Air	9.0
Foam-CO_2	5	0.25	CO_2	6.5

2.3 Methods

A series of laboratory experiments were carried out to investigate the effect of CO_2 on the stability of the foam and the encapsulated CO_2 in the foamed backfill material and its underlying strengthening evolution mechanisms. The overall experimental procedure is illustrated in Fig. 1.

2.3.1 *Foamed stability*

Foam stability was measured following the Chinese measurement standard (JC/T 2199-2013), where the drainage of the prefabricated foams was evaluated. The mass of the liquid draining from the bottom of the foam was recorded at successive times. The drainage (ε_t) was then determined by Eq. 1, as follows:

Table 3 Experimental scenarios

No	Target density (kg/m^3)	Fly ash (g)	Cement (g)	SS (g)	Water (g)	L/S	Foam (mL)	Dry density (kg/m^3)
CFB-2	600	1,133.8	283.4	56.7	566.8	0.4	200	621 ± 5
CFB-4	500	1,124.6	281.2	56.2	562.2	0.4	400	506 ± 5
CFB-6	400	1,115.4	278.8	55.8	557.8	0.4	600	424 ± 5
AFB-2	600	1,133.8	283.4	56.7	566.8	0.4	200	652 ± 10
AFB-4	500	1,124.6	281.2	56.2	562.2	0.4	400	546 ± 10
AFB-6	400	1,115.4	278.8	55.8	557.8	0.4	600	451 ± 10

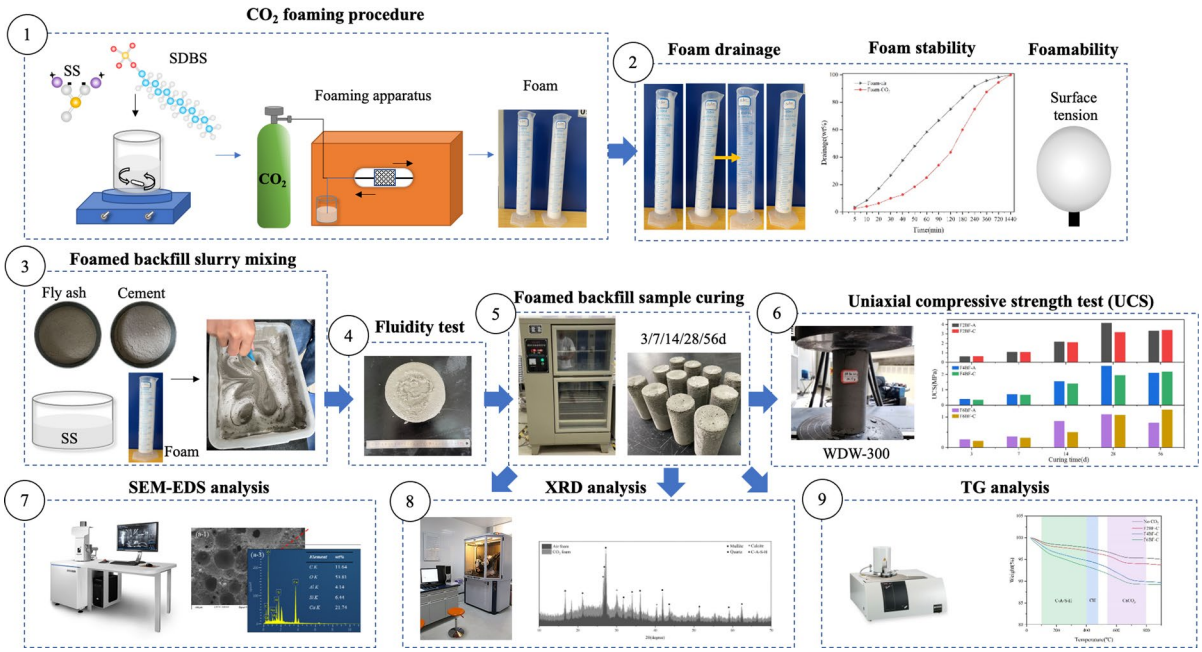

Fig. 1 Schematic representation of the study

$$\varepsilon_t = \frac{m_t}{\rho_a \mathrm{V}} \tag{1}$$

where m_t is the mass of the foaming agent solution discharged after t min, ρ_a is the density of the foam and V is the volume of the measuring container.

2.3.2 *Properties of foaming agent*

The prefabricated foams were measured to their density using a liquid displacement pycnometer at room temperature, where each sample was measured three times and the average value is presented in the final value. The foaming ability was evaluated by measuring the foaming multiple using a method based on the Chinese standard "Foamed concrete" (JG/T 266-2011). Prior to measurement, a freshly prepared foam was added into a bottom less glass barrel of 250 mL volume and 60 mm diameter and weighed. The calculation formula of foaming multiple was given in Eq. 2, as follows:

$$\mathrm{M} = \frac{\mathrm{V}}{\left(\mathrm{G}_2 - \mathrm{G}_1\right)/\rho} \tag{2}$$

where M is the foaming multiple of prefabricated foam, V is the volume of a bottomless glass bucket (mm^3), G_1 is the quality of a bottomless glass bucket (g), G_2 is the total mass of bottomless glass drums and prefabricated foam (g), ρ is the density of an aqueous foaming agent (g/mm^3). The foaming multiple of the sample was measured three times, and three measurements were averaged to give the final result.

The surface tension of the foams was measured using DropMaster DMs-401(Kyowa Interface Science Co., Ltd., Tokyo, Japan) at room temperature. The viscosity of the foam was measured using NDJ-1 rotary viscometer with a range of 1–105 mPa·s and a precision of ± 1%

2.3.3 *Fluidity of fresh foamed backfill materials*

The fluidity of each foamed backfill slurry was measured using a clean and dry truncated cone with a top diameter of 50 mm, a bottom diameter of 100 mm, and a height of 150 mm, and its inner wall was smooth. The cone was kept steadily on a plate while the prepared foamed backfill was poured into the die. The overflow was cut off with a scraper, and then the die was gently lifted vertically to allow the slurry to spread freely. After 60 s, the diameter of the slurry

was measured as the fluidity of the foamed backfill. The fluidity test was performed following the GB/T 50080-2016 standard from the Chinese National Standardization Commission (Zhang et al. 2022). The aforementioned process was repeated three times, and the fluidity of fresh foamed backfill slurry was the average of the three experimental results.

2.3.4 *Properties of hardened foamed backfill materials*

The foamed backfill specimens were subjected to uniaxial compressive strength (UCS) tests after reaching the regarding curing time. The test was carried out in accordance to the Chinese standard "Test Methods of Autoclaved Aerated Concrete" (GB/T11969-2008) (Wang et al. 2018) using a WDW-300 electronic universal testing machine. Displacement loading at a constant speed of 1 mm/min to the cured specimens. The peak stress and displacement of each sample were recorded during the entire load failure specimens, the UCS after 3, 7, 14, 28, 56 d of curing were determined. All tests were repeated three times and the average UCS value was calculated for further analysis.

2.3.5 *Microstructural analysis of the foamed backfill materials*

A small portion of the sample was collected during the UCS experiment. Hydration was stopped with anhydrous ethanol, and agate was ground to less than 200 mesh. After that, the samples were dried at 50 °C for 24 h. XRD test were performed to analyze the hydration products of the foamed backfill specimens. The crushed sample also underwent SEM and EDS analyses using a field emission microscope (Hitachi model Regulus 8100) with an energy-dispersive spectrometer (EDXA model 560) to determine its micromorphology and structural characteristics. The process to stop the hydration, grinding, and drying was the same for SEM and XRD analyses, except that the surface of the SEM sample was sprayed with gold.

2.3.6 *CO_2 uptake*

The CFB sample at different CO_2 foam content was collected after 56 d curing to measure the $CaCO_3$ content using thermogravimetric (TG, Thermoplus Evo TG 8120, Rigaku, Japan) analysis. The test was performed from 30 to 1000 °C with an increased heating rate of 10 °C/min at an air flow rate of 200 mL/min. The CO_2 uptake was calculated as follows:

$$W_{\mathrm{CO_2}} = \frac{W_{\mathrm{CaCO_3,f}} - W_{\mathrm{CaCO_3,i}}}{100} \times \frac{M_{\mathrm{CO_2}}}{M_{\mathrm{CaCO_3}}} \times W_{\mathrm{solid}} \quad (3)$$

where W_{CO_2} is the amount of adsorbed CO_2 in CFB material (mg-CO_2/g-CFB), $W_{CaCO_{3,i}}$ is the initial amount of $CaCO_3$ in the un-CO_2 reacted sample, $W_{CaCO_{3,f}}$ is the amount of $CaCO_3$ in the CFB sample, M_{CO_2} and M_{CaCO_3} are the molar mass of CO_2 and $CaCO_3$, respectively, and W_{solid} is the mass of the solid sample. The calculation of CO_2 uptake is based on the mass balance principle, where it is assumed that the decomposition of $CaCO_3$ is the only process that occurred in the given temperature range (540–800 °C) and CO_2 is the only gas emitted from the solid sample in the mentioned temperature range.

3 Results and discussion

3.1 Properties of foams

3.1.1 *Foam stability*

After formulation, foam starts to coalesce and gradually coarsens due to gravity and van der Waals forces. This eventually leads to gas diffusion and bubble rupture. This implies that the control of the liquid foam film is an important parameter in foam stability. Figure 2a illustrates the drainage volumes of air and CO_2 formulated foams after 60 min. In the first 5 min, the drainage volume of air foam was 10 mL, whereas only 7.5 mL was drained from the CO_2 foam. The drainage volume of air foam continued to increase 17 mL and 25 mL after 20 and 60 min, respectively. It is noticeable that the drainage of CO_2 foam reached an equilibrium point after 20 min (12.5 mL), and gradually increased to 15 mL after 60 min. These results indicate CO_2 has a positive effect on the drainage of fabricated foam.

The dynamic viscosity of the air and CO_2 foams was measured immediately after formulation, as shown in Fig. 2b. Within the initial 10 min, both foams presented similar behavior, where the viscosity was approximately 5 mPa·s. The viscosity of the CO_2

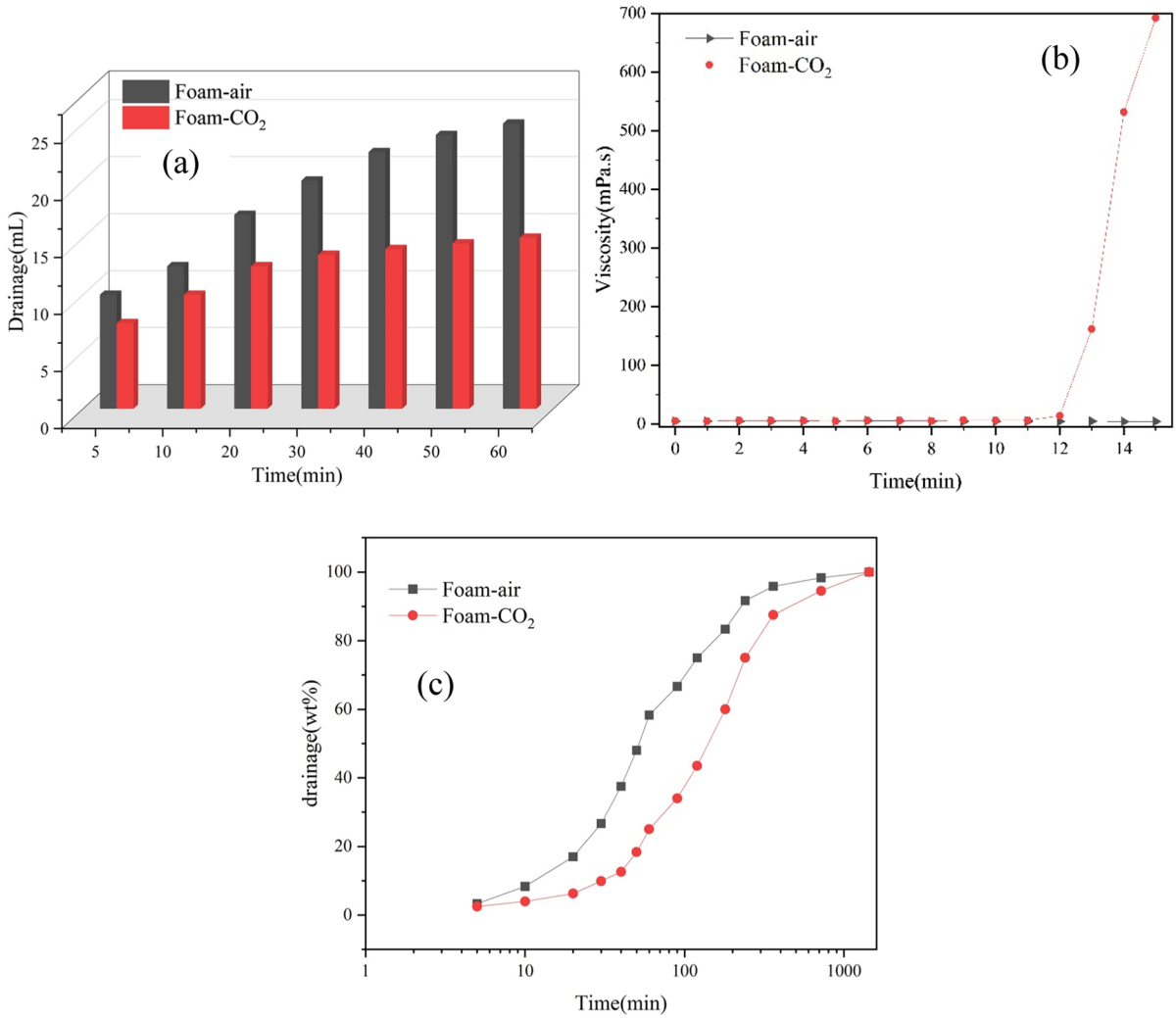

Fig. 2 Stability of formulated foams by air and CO_2: **a** drainage volumes of foam over 60 min, **b** dynamic viscosity of foams and **c** foam drainage

foam gradually increased to 14.2 mPa·s after 12 min, and reached 692 mPa·s at 15 min, whereas no increment was found in air foam. The increased viscosity slowed the loss of liquid film, thus increasing the strength of the foam film and the stability of the foam (Wang et al. 2019). The changes in the foam drainage of both foams over time are given in Fig. 2c. It clearly shows that CO_2-carrying foams underwent little drainage and foam loss within 30 min, whereas air foam exude more liquid. CO_2 foam exhibited a drainage rate of only 60% after 180 min. Furthermore, CO_2 foam remained more than air foam by about 16% and 8% after 240 and 360 min, respectively.

Figure 3a presents the images of foams developed by different gases at initial and 60 min after preparation. Immediately after preparation, both foams had identical volumes. After that, some liquid gradually drained from the foams. The liquid drained continuously decreased with encapsulated CO_2. A large volume of air foam collapsed after 60 min, whereas the CO_2 foam showed fewer collapses and maintained most of its shape. The reduction in drainage and the collapse of the foam with CO_2 are attributed to the formation of a gel film that encapsulated and stabilized the bubbles in the foam. It was proved in the reaction test between SS and CO_2, where the SS

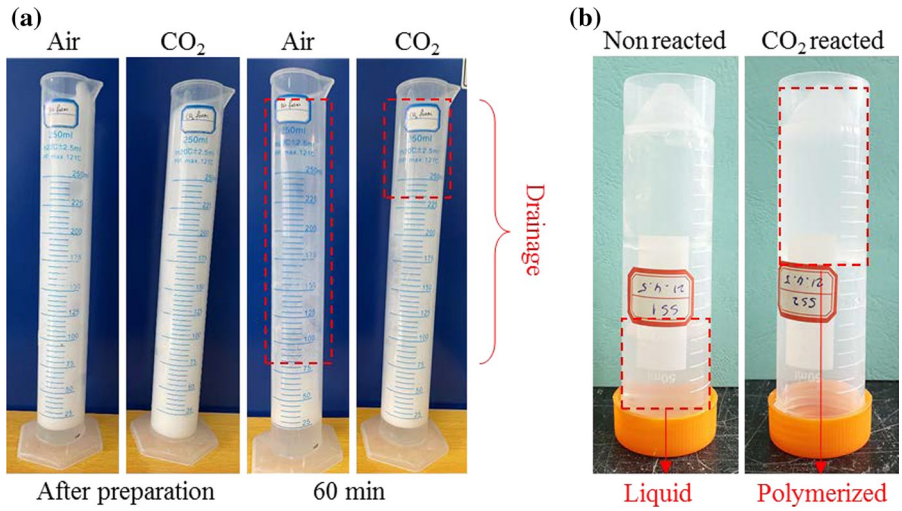

Fig. 3 **a** Images of the foams produced by air and CO_2. **b** Images of foaming solution reacted to CO_2

liquid began to polymerize approximately 10 min after CO_2 injection (Fig. 3b).

3.1.2 Foam ability

The enhanced stability foam by injected CO_2 was further discovered, where foaming solution was allowed to react to CO_2 for 10 min at ambient conditions during surface tension test. Figure 4a presents the dynamic surface tension of the CO_2-reacted foaming solution, where the surface tension is the tension force generated by the spontaneous shrinkage of a liquid surface and thus represents the van der Waals force between molecules on the surface. The generation of bubbles is closely related to the surface tension of a liquid, since the higher the surface activity of a liquid, the lower its surface tension, and thus the more bubbles will be generated. The surface tension of water is 70.2 mN/m, which is not conductive to the generation of foams. The surface tension was reduced to 30.5 mN/m by SDBS treatment, allowing dense foams to be generated. As shown in Fig. 4a, the surface tension of CO_2-reacted foaming solution was 25.6 mN/m after 10 min, indicating that the formation of gelling agent further enhanced the surface activity of SDBS. The same observation was found

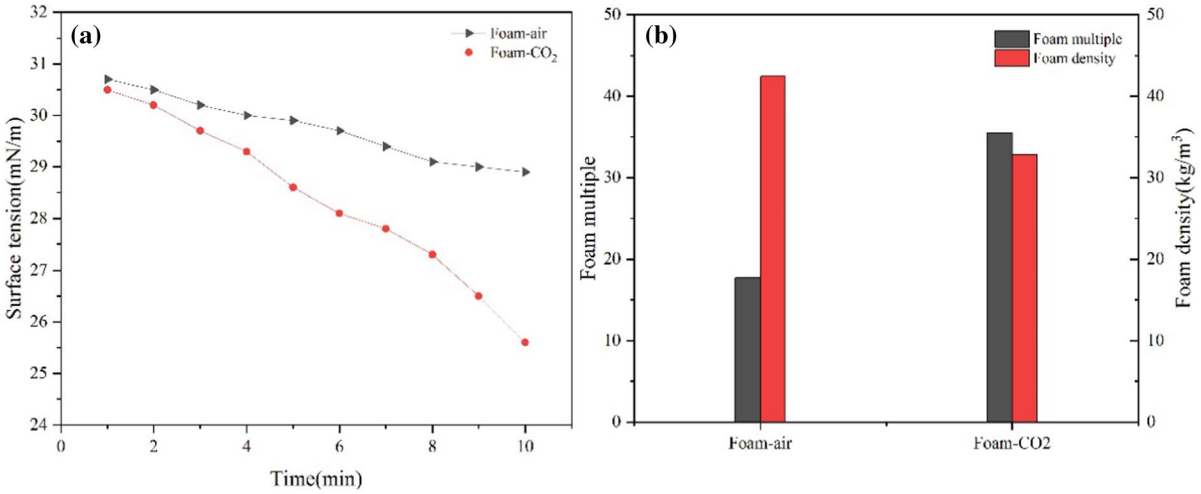

Fig. 4 Effect of CO_2 on the foam ability of the foaming liquid: **a** surface tension of the foaming liquid and **b** foaming multiple and density of the prefabricated foam

in literature (Stubenrauch et al. 2000). The continued decrease in surface tension has a positive effect on the spread of the forming gel, which works as a thermodynamically stable film at the liquid–vapor interface (Haller et al. 2013). The density and foaming multiple of prefabricated foams using air and CO_2 are given in Fig. 4b. The results indicated that the foaming multiple of CO_2 foam was approximately 50% higher than which of air foam. The foam density of CO_2 foam was 32.8 kg/m_3, which was about 30% less than that of air foam. The reduction in density was caused by the reaction between CO_2 and SS that resulted in a large number of thin films covering the generated bubble, thus reducing the surface tension at the vapor–liquid interface. The described phenomenon facilitated the generation of foam, thereby increasing the foaming multiple. Consequently, more bubbles were developed per unit volume of foaming liquid.

3.1.3 Foam stabilization mechanisms

Foam is a metastable system where its structure and properties change over time in an irreversible manner (Yekeen et al. 2017). Foam instability in an open system is controlled by three interdependent mechanisms: (i) foam drainage due to gravity, (ii) bubble coalescence due to the rupture of liquid films between the neighboring bubbles, and (iii) coarsening due to capillary pressure differences inducing the transfer of gas between bubbles (Yu and Kanj 2022). These mechanisms affect the strength of a bubble film and the interaction between the films and the Plateau borders. Therefore, increasing the interfacial strength of a bubble surface and controlling Plateau borders increase bubble stability. Figure 5 describes the mechanism by which the gel inclusion film stabilized the bubbles. After CO_2 reaction, a double layer structure of gel was formed, that prevented the flow of liquid and slowed the expulsion of bubbles.

In the liquid film of foam, the encapsulated CO_2 reacts to SS to form a gel network with high water retention, which tightly wrapped the gas and formed the colloidal shell structure on the surface of bubbles as shown in Fig. 6. Water was distributed inside the network structure, which reduced the speed of liquid drainage due to gravity, agreeing with the results in Fig. 2. Moreover, the gel structure also increased the viscosity of the continued phase solution in Plateau borders area and node positions, significantly increasing the flow resistance of the liquid in foam, thereby reducing the drainage rate of the liquid from the foam system, as well as improving the water retention time and the stability of foam system. Gelified foam films could reduce the coalescence and rupture rate of gel-stabilized foam (Rio et al. 2014). In the foam system, the gel network structure connected all bubble liquid films, Plateau borders, and nodes into a whole, forming a viscoelastic three-dimensional network skeleton to support the entire foam system as seen in Fig. 5b, which could maintain the thickness of liquid film for a long time and enhance the mechanical strength of foam film. When the foam was affected by other external factors, the whole structure was beneficial for the foam to maintain dimensional stability. Furthermore, during the foam drainage process, the liquid phase slowly moved in an approximate three-dimensional overall form, which could ensure the uniform thickness of the foam film to avoid the rupture caused by differences in the loss of the liquid phase in different areas of the liquid film. The connected bubbles in

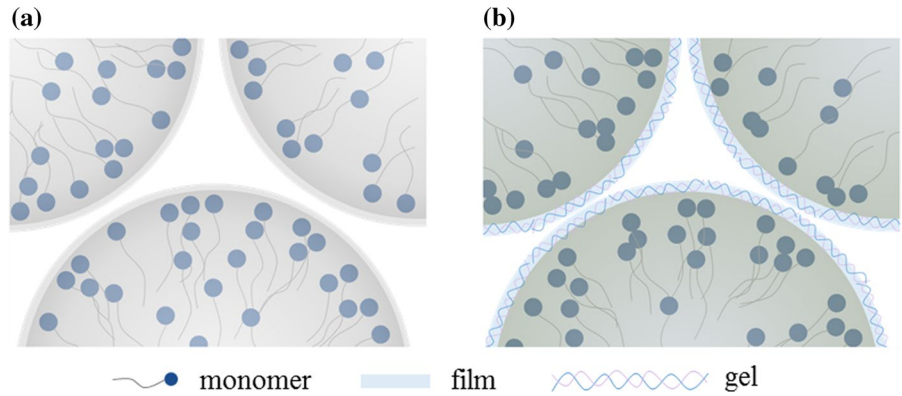

Fig. 5 Structural schematic representation of **a** foam-air and **b** foam-CO_2

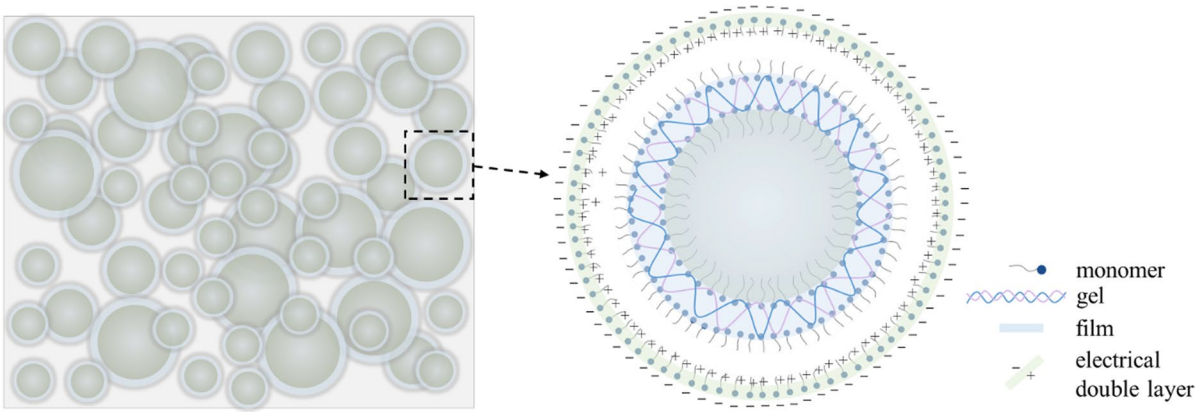

Fig. 6 Schematic illustration of single bubble structure in foam-CO_2

the foam finally strengthened the overall dimensional stability of the gel-stabilized foam.

3.2 *Effect of CO_2 foam on foamed backfill materials*

3.2.1 Slake characteristics

Figure 7 shows the measured fluidity of the fresh air and CO_2 foamed backfill materials, scaled in slump value. The fresh slurry of the air foamed backfill presents a higher slump value than CO_2 case, and the increment increases with adding foam volume. This can be attributed to the low strength of the air bubble film and the large volume of free water around the foam, which is partially generated in the foam ablation process and the increased mobility of the backfill slurry. In comparison, the foam containing CO_2 had a higher viscosity and less water was lost by drainage; thus, foamed backfill materials prepared from CO_2 generation exhibited lower fluidity than that prepared from air.

3.2.2 Mechanical properties of hardened foamed backfill materials

The uniaxial compressional strength (UCS) of the hardened foamed backfill samples were determined at 3, 7, 14, 28 and 56 d as shown in Fig. 8.

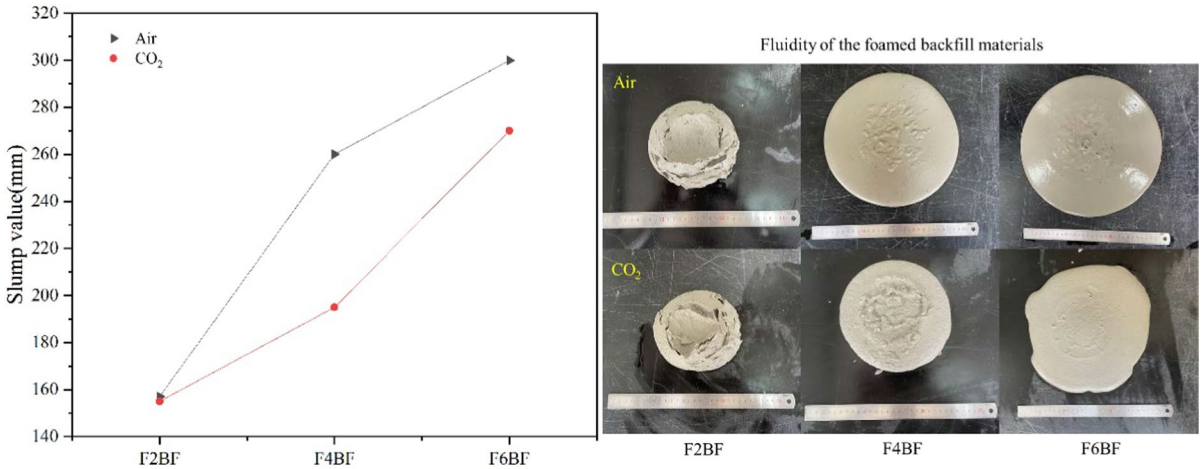

Fig. 7 Measured fluidity of foamed backfill materials

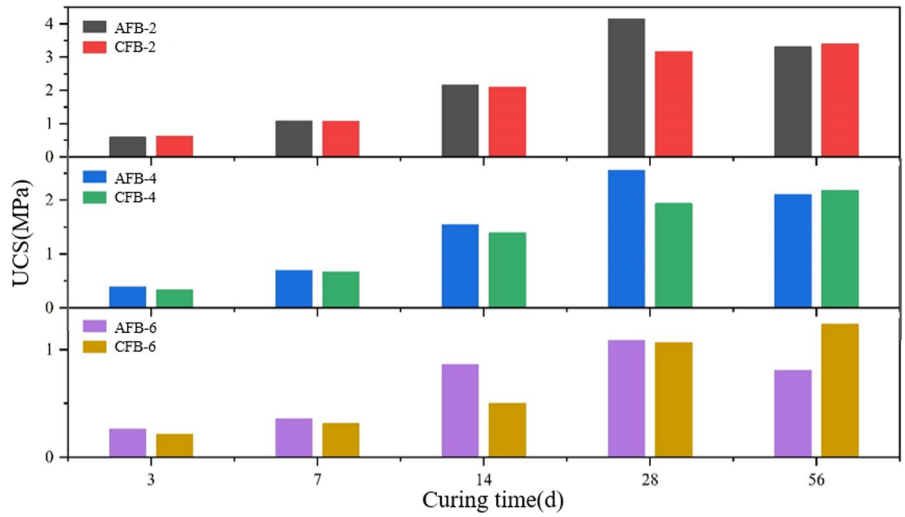

Fig. 8 UCS of foamed backfill materials prepared using air and CO_2 foams

The UCS of all samples, which have an actual dry density of approximately 400, 500 and 600 kg/m_3, based on the volume of the foam carried, increased with curing time. From 3 to 28 d, the strength of the air foamed backfill materials was higher than that of CO_2. For instance, the 28 d UCS of AFB-2 was 4.15 MPa, which was 23.6% greater than CFB-2. This was identical for every foam volume case. However, it was noticed that when the curing time increased to 56 d, the UCS of air foamed backfill declined, while which of CO_2 incremented. The measured degree of increased UCS by CO_2 foam was 2.7%, 3.6% and 34.7% corresponding to CFB-2, CFB-4 and CFB-6, respectively.

3.2.3 Microstructural evolution of hardened foamed backfill materials

Foamed backfill carries many closed pores provided by stable foam, so its strength is significantly related to the porous medium within and the support provided by pore wall. As provided in Table 3, the density of the foamed backfill samples prepared with air foam had a higher dry density regardless of the proportion of foam volume. This well explains its greater UCS in curing no more than 28 d. Microstructures of the air and CO_2 foamed backfill materials measured by SEM and EDS spectrum analysis, are shown in Fig. 9, to discover the underlying mechanisms. As observed, CO_2 foamed backfill material has a more uniform pore structure than which of air case (Fig. 9a-1 and b-1). Calcium hydroxide (CH) formed within the capillary pore of the air foamed backfill material due to the added cement. With the addition of fly ash, Al_2O_3 reacts with CH in a pozzolanic reaction to develop a hydration product of calcium aluminosilicate hydrate (C-A-S-H) on the inner pore walls. Figures 9a-3 and b-3 dedicate the corresponding EDS spectra of the chemical composition of C-A-S-H inside the pores. After 56 d curing, the Ca/(Si + Al) ratios of C-A-S-H of air and CO_2 foamed backfill material was calculated to be 0.17 and 0.39, respectively. As addressed in literature (Ngo 2023), the lower Ca/(Si + Al) ratio indicates greater amount of C-A-S-H gel is developed and vice versa. As the presented morphology of the air foamed backfill in Fig. 9a-2, its mechanical properties depended largely on C-A-S-H gel and CH. On the other hand, the encapsulated CO_2 within the close pore of CO_2 foamed backfill material reacted with hydration products of C-A-S-H and CH during hydration process. As shown in Fig. 9b-2, CH was consumed in a carbonation reaction (Eq. 4) and $CaCO_3$ was then produced (Fig. 9b-4). Incorporating the increased Ca/(Si + Al) ratio, the strength development in CO_2 foamed backfill material depend on the filling effect of $CaCO_3$. The comparison of the microstructural evolution of the air and CO_2 foamed backfill material is given in Fig. 10. It clearly shows that the filling effect of $CaCO_3$ reduced the cracks in the pore wall in the foamed backfill material, increasing the hardness of the pore wall, thus increasing the strength of the foamed backfill materials

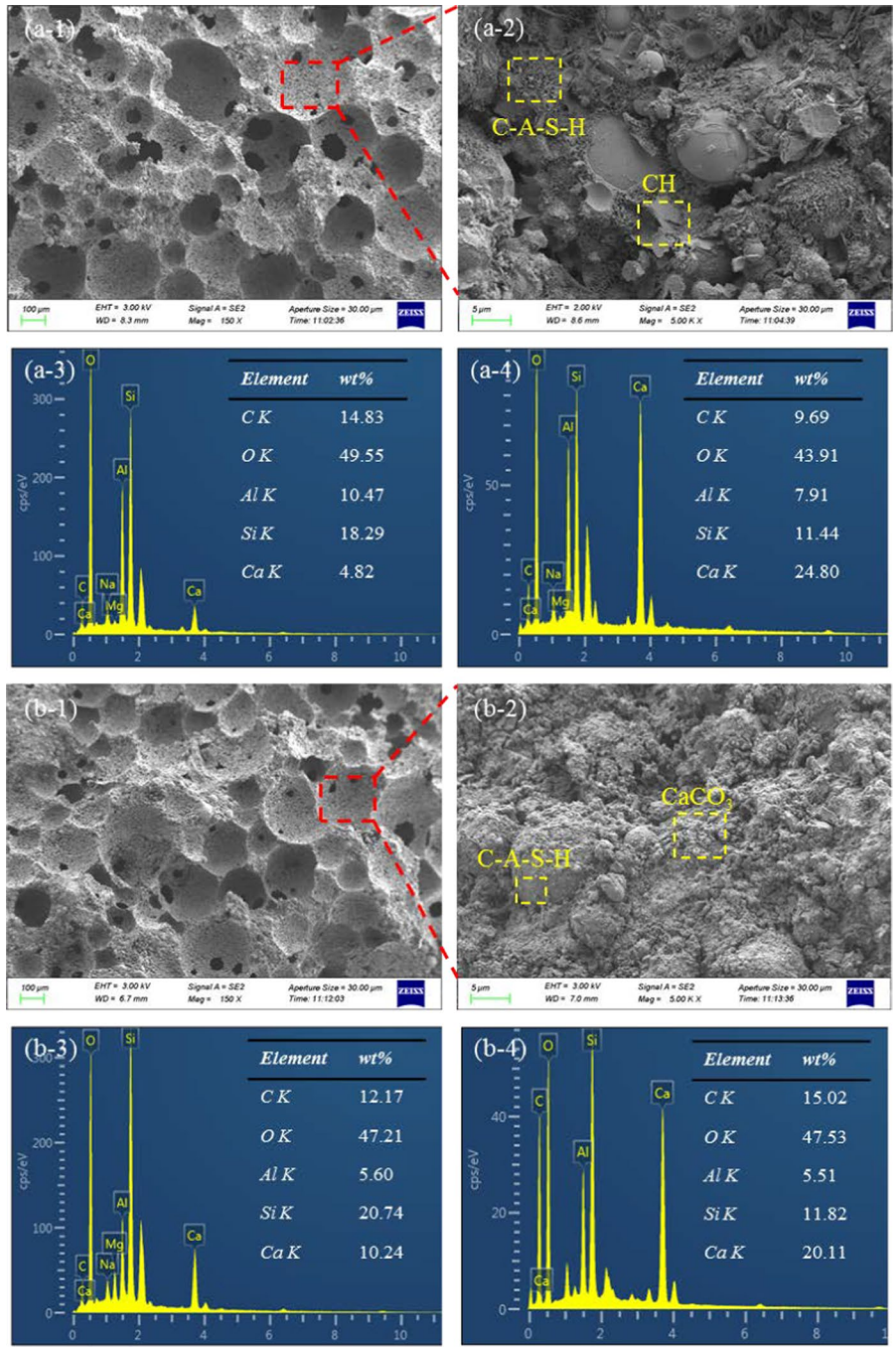

Fig. 9 Internal pore wall morphology (**a**-1), hydration products (**a**-2), EDS spectrum of C-A-S-H (**a**-3) and EDS spectrum of CH (**a**-4) of air foamed backfill material, internal pore wall morphology (**b**-1), hydration and carbonation products (**b**-2), EDS spectrum of C-A-S-H (**b**-3) and EDS spectrum of $CaCO_3$ (**b**-4) of CO_2 foamed backfill material

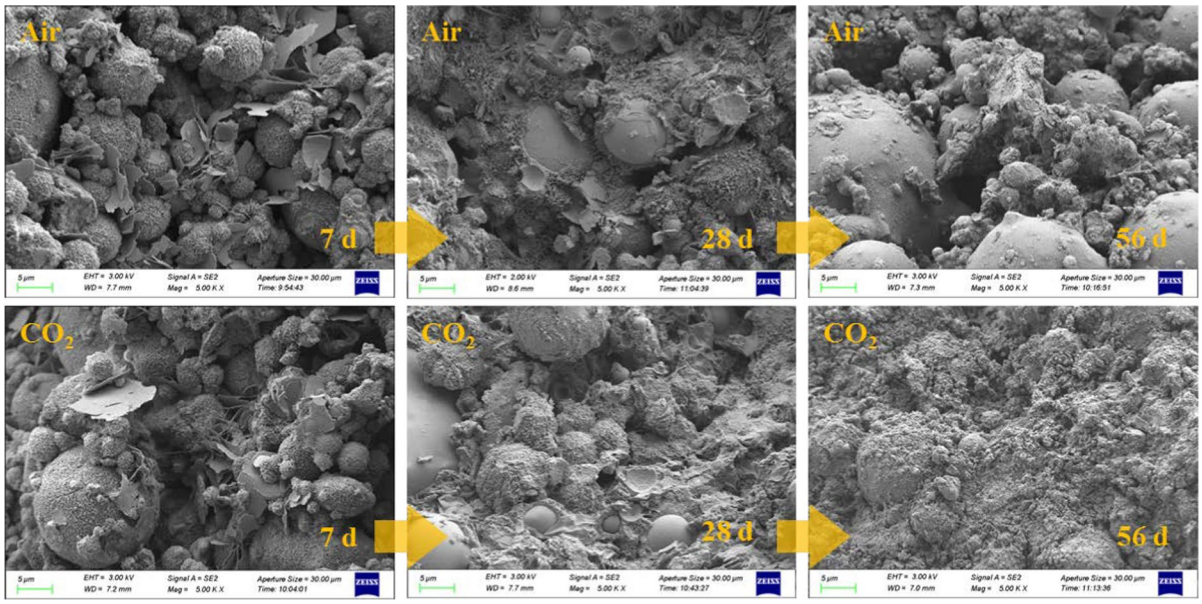

Fig. 10 Microstructural evolution of pore wall of air and CO_2 foamed backfill material

$$Ca(OH)_2 + CO_2 \rightarrow CaCO_3 + H_2O \quad (4)$$

3.2.4 *Mechanism of pore structure in foamed backfill materials*

Unlike ordinary backfill material, foamed backfill material has many closed pores that occupy up to 75–85% of its total volume. Therefore, the properties of foamed backfill depend more on the pore structure than on the cementitious matrix. The XRD spectra of the pore structure are then postulated as shown in Fig. 11.

It can be seen that the XRD spectrum mainly comprises diffraction peaks of mullite, calcite, quartz and C-A-S-H gel. Among which, mullite and quartz were originated from fly ash, while calcite was produced in the carbonation reaction. The XRD peak intensity of $CaCO_3$ in the CO_2 foamed backfill material is higher than which in air foamed case. This is consistent with the SEM–EDS investigation. Furthermore, the XRD spectrum of the CO_2 foamed backfill material have a broader band than air foamed case at $2\theta = 15–30°$, indicating a greater amorphous phase in the pore structure. Therefore, the evolution of porosity and strengthen mechanism of pore structure in the foamed backfill prepared by CO_2-encapsulate foam

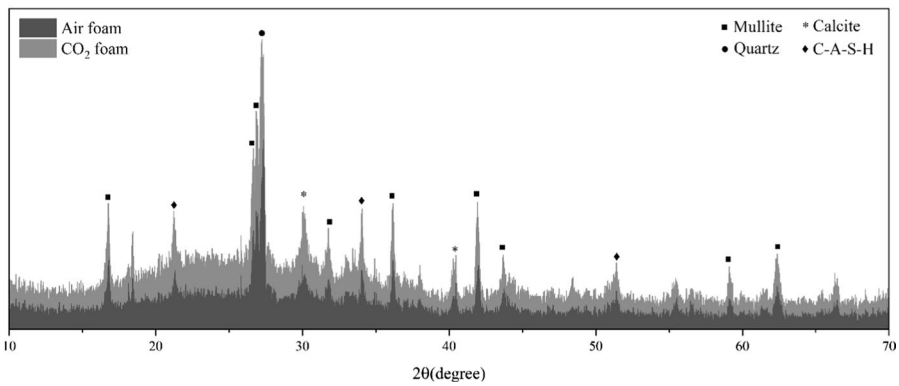

Fig. 11 XRD spectra of foamed backfill materials using air and CO_2

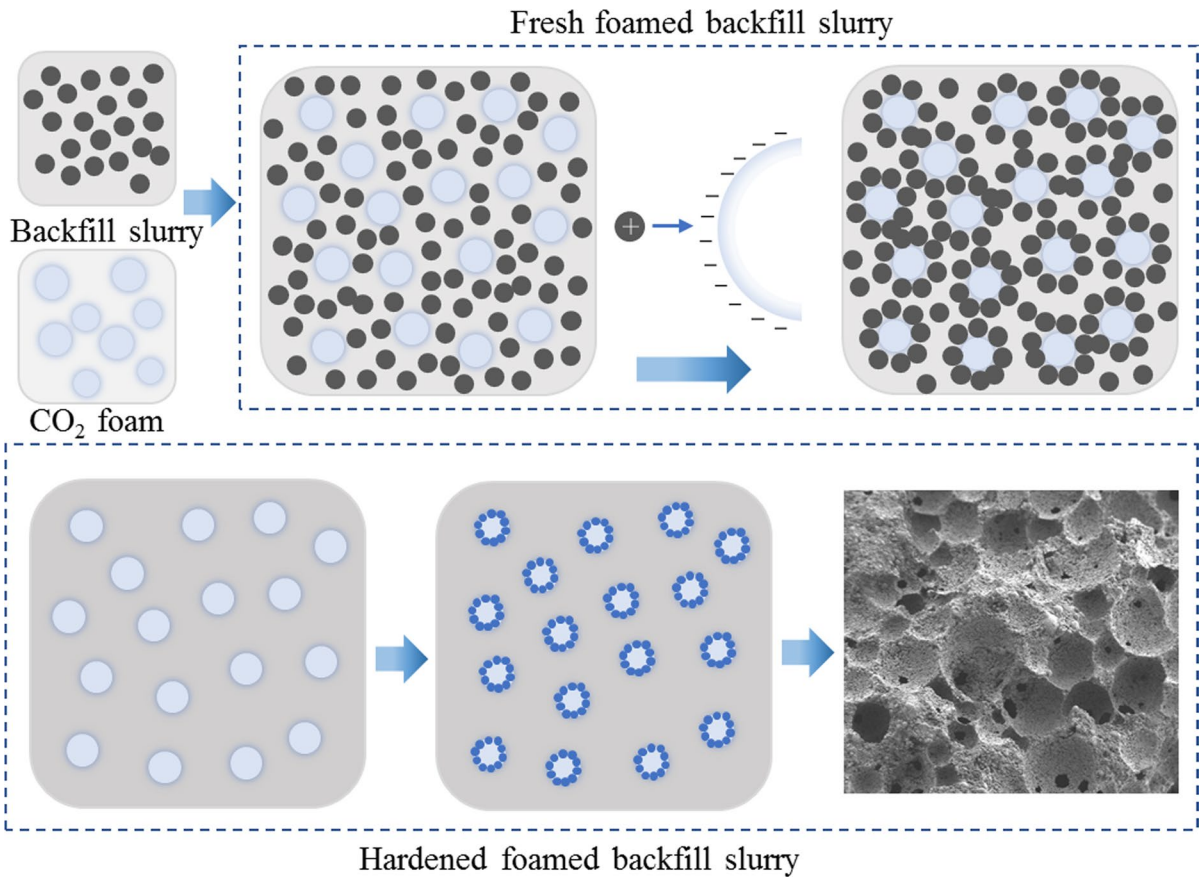

Fig. 12 Schematic diagram of the evolution of the pore structure in CO_2 foamed backfill materials

modification is shown in Fig. 12. After the backfill slurry was mixed with the CO_2 foamed, the cationic backfill particles and the anionic gel network spreading on the surface of the bubble associated. This strengthened the bubbles and mitigated the bubble breakage during the subsequent mixing process. Over time, backfill particles attached to bubble films gradually formed a gelatinous substance that encapsulated entire bubbles (Guo et al. 2023b).

The formation of closed pores is closely related to the stability of the prefabricated foam. As mentioned above, the strength of the foam films was significantly increased by the gel network developing in a sodium silicate-CO_2 reaction, as this caused the formation of near-spherical pores and a more uniform pore wall. During the hydration process, the encapsulated CO_2 continuously reacted to hydration products in which $CaCO_3$ particles developed and migrated to gel film and were deposited on the walls of the pores. The smaller particles of $CaCO_3$ filled and coated the inner walls of the pores. This increased the pore wall strength and thus stabilized the foamed backfill material.

3.3 *CO_2 uptake*

Figure 13a shows the thermogravimetric curve of the foamed backfill material. The main weight loss temperature ranges are in the range of 100–400 °C, 400–480 °C and 540–800 °C, that are representing the dehydration of C-A-S-H gels, dehydrogenation of CH and decomposition of $CaCO_3$, respectively (Ta et al. 2023). Figure 13b shows the effects of carbonation by CO_2 foam in different content on the amount of sequestrated CO_2 and the resulted strength enhancement. As indicated, as the amount of CO_2 foam increases, the sequestration of CO_2 within the foamed backfill materials, which was 5.6, 7.5 and

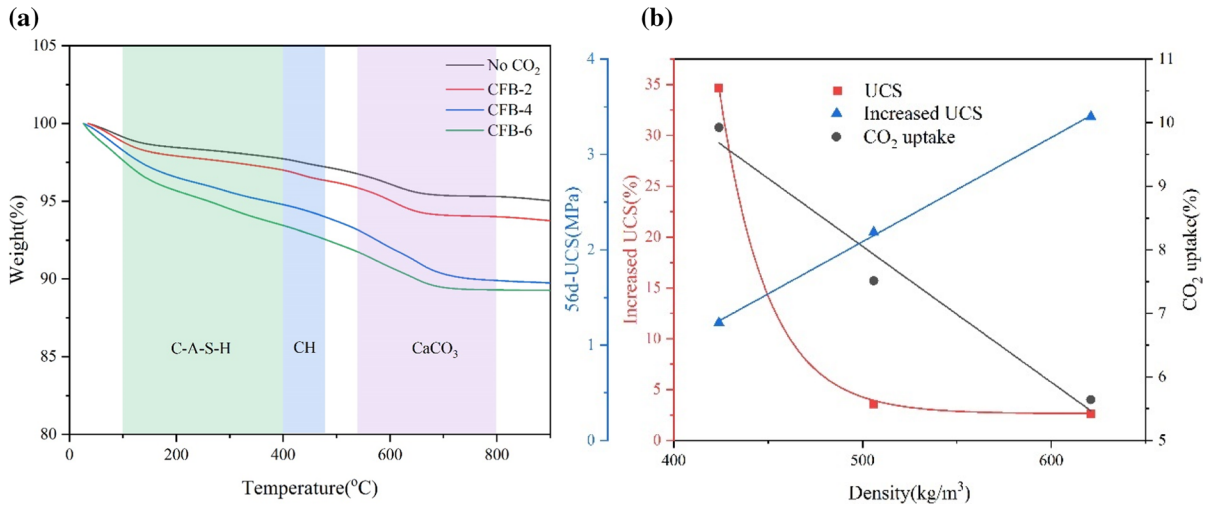

Fig. 13 **a** Plots of TG as function of temperature for different foam content, **b** plots of UCS, increased UCS and CO_2 uptake at 56 d as a function of dry density

9.9% for CFB-2, CFB-4 and CFB-6, respectively. Furthermore, it can be inferred that as the dry density increases, the strength of CO_2 foamed backfill material exhibits an upward trend and the amount of CO_2 sequestration shows a downward trend overall. In mine filling, the maximum strength and carbon sequestration is desired while minimizing density to optimize the economic viability of the technique. For this purpose, a reasonable intersection point is plotted in Fig. 13b, and the plotted point corresponds to the optimal density value of 498 kg/m^3. In this study, the closest composition to this point is CFB-4 with a strength of 2.18 MPa, which can sequester 27.4 kg of CO_2 per 1 ton of backfilling. However, if an increase in UCS is considered, the intersection moves closer to the CFB-6 material. In this case, up to 36.2 kg of CO_2 can be sequestered by 1 ton of backfilling, and approximately 35% of the strength increased over the air foamed backfill material. The study listed above shows that it is feasible to prepare foamed backfill material for mine filling for in-situ sequestration and utilization of CO_2.

4 Conclusions

In this study, a novel highly stable foam was prepared by introducing CO_2 and sodium silicate into a foaming agent, and the effect of developed gel network on the stability of the fresh foam system was discussed. The present study resolved the issue of limited application of aqueous foam in backfill material due to its thermodynamically instability. The plateau borders structure of the foam system was effectively controlled by a polymerization of sodium silicate by CO_2 in a sol–gel reaction, which improves the stability performance of the foam. The properties and microstructure of the foam were investigated and the mechanical properties and durability of the foamed backfill material were improved by stable CO_2 foam. The following conclusions can be drawn:

(1) The introduction of CO_2 and sodium silicate into foam blocked the Plateau borders which had a significant effect on the coarsening of water-based foam. A double layer gel formed at the liquid film of the CO_2 foam that keeping the drainage rate after 180 min for only 60%.
(2) When the foam contained an appropriate proportion of gel network after being exposed to CO_2, gel adsorbed onto the foam walls due to viscoelastic three-dimensional network skeleton. This resulted in the formation of a double-layered core–shell structure of the single bubble, which increased the stability of the foam.
(3) Highly stable foam improved the mechanical properties of foamed backfill material. The encapsulated CO_2 in the pore reacted to C-A-S-

H and CH to produce micro $CaCO_3$ particles that attached to the pore wall and uniformly filled the micro cracks, thus increased the strength of the foamed backfill material. The increased UCS of the foamed backfill material prepared using highly stable CO_2 foam was 35% above that of the air foam.

(4) CFB enables CO_2 sequestration in backfill materials in the form of CO_2 foam at ambient condition, where up to 36.2 mg-CO_2/g-CFB.

Acknowledgements The authors appreciate the National Natural Science Foundation of China, grant number 52250410338, National Natural Science Foundation of China, grant number 51874280, Foundation Research Funds of the Central Universities, grant number 2021ZDY0211, and Foundation of the National Natural Science Foundation of China, grant number 51974328 for financial support.

Author contributions Ichhuy Ngo, conceptualization, methodology, funding acquisition, formal analysis, investiga-tion, writing original draft, writing review and editing, visualization; Liqiang Ma, Conceptual-ization, methodology, funding acquisition; Zhiyang Zhao, data curation, writing review and ed-iting; Jiangtao Zhai, data curation, writing review and editing; Kunpeng Yu, data curation, writ-ing review and editing; Yonghui Wu, funding acquisition, writing review and editing.

Funding Funding was supported by National Natural Science Foundation of China (52250410338), National Natural Science Foundation of China (51874280), Foundation Research Funds of the Central Universities (2021ZDY0211), and Foundation of the National Natural Science Foundation of China (51974328).

Data availability Data available on request from the authors.

Declarations

Competing interests The authors declare no competing interests.

Ethics approval No ethical approval was necessary for this work.

Consent to publish The authors confirm that this work is original and has not been published before.

Conflict of interest The authors declare no competing interests.

References

Asghar U et al (2021) Review on the progress in emission control technologies for the abatement of CO2, SOx and NOx from fuel combustion. J Environ Chem Eng 9(5):106064

Bakonyi P et al (2020) Possibilities for the biologically-assisted utilization of CO2-rich gaseous waste streams generated during membrane technological separation of biohydrogen. J CO2 Util 36:231–243

Chen Y-G et al (2021) Foamed concrete containing fly ash: properties and application to backfilling. Constr Build Mater 273:121685

Guan L-L et al (2023) Foamed concrete utilizing excavated soil and fly ash for urban underground space backfilling: physical properties, mechanical properties, and microstructure. Tunn Undergr Space Technol 134:104995

Guo W et al (2023a) CO2 emissions retrieval from coal-fired power plants based on OCO-2/3 satellite observations and a Gaussian plume model. J Clean Prod 397:136525

Guo S et al (2023b) Nanoparticle-stabilized foam with controllable structure for enhanced foamed concrete. Constr Build Mater 362:129723

Haller PD, Bradley LC, Gupta M (2013) Effect of surface tension, viscosity, and process conditions on polymer morphology deposited at the liquid-vapor interface. Langmuir 29(37):11640–11645

Li Z et al (2023) Evaluation on direct aqueous carbonation of industrial/mining solid wastes for CO2 mineralization. J Ind Eng Chem 122:359–365

Liu X et al (2022) Comparison of SDS and L-Methionine in promoting CO2 hydrate kinetics: implication for hydrate-based CO2 storage. Chem Eng J 438:135504

Liu Y-L et al (2023) Production and performance of CO2 modified foam concrete. Constr Build Mater 389:131671

Miao X et al (2020) Characterisation of wellbore cement microstructure alteration under geologic carbon storage using X-ray computed micro-tomography: a framework for fast CT image registration and carbonate shell morphology quantification. Cement Concr Compos 108:103524

Miao E et al (2023) Kinetic analysis on CO2 sequestration from flue gas through direct aqueous mineral carbonation of circulating fluidized bed combustion fly ash. Fuel 342:127851

Ngo I et al (2020) Formation damage induced by water-based alumina nanofluids during enhanced oil recovery: influence of postflush salinity. ACS Omega 5(42):27103–27112

Ngo I et al (2022) Experimental investigation of CO2-induced silica gel as the water blocking grout effect of aquifer ions. ACS Omega 7(31):27090–27101

Ngo I et al (2023) Durability of CO2-fly ash-based backfill materials in cation water deterioration. Int J Min Reclam Environ. https://doi.org/10.1080/17480930.2023.2216498

Ngo I et al (2023a) Enhancing fly ash utilization in backfill materials treated with CO2 carbonation under ambient conditions. Int J Min Sci Technol 33(3):323–337

Ngo I et al (2023b) Effect of the co-activation of sodium silicate and CO2 on setting and mechanical properties of coal gangue-fly ash backfill (CGFB). Environ Earth Sci 82(7):190

Ostovari H et al (2023) Towards a European supply chain for CO2 capture, utilization, and storage by mineralization: insights from cost-optimal design. J CO2 Util 72:102496

Pan S-Y et al (2018) An overview: reaction mechanisms and modelling of CO2 utilization via mineralization. Aerosol Air Qual Res 18(4):829–848

Power IM et al (2021) Carbonation, cementation, and stabilization of ultramafic mine tailings. Environ Sci Technol 55(14):10056–10066

Ren J et al (2023) Roles of montmorillonite clay on the kinetics and morphology of CO2 hydrate in hydrate-based CO2 sequestration1. Appl Energy 340:120997

Rio E et al (2014) Unusually stable liquid foams. Adv Coll Interface Sci 205:74–86

Stubenrauch C et al (2000) Polymer/surfactant complexes at the water/air interface: a surface tension and X-ray reflectivity study. Langmuir 16(7):3206–3213

Ta X et al (2023) Effect of carbonation and foam content on CO2 foamed concrete behavior. J Market Res 23:6014–6022

Wang C-Q et al (2018) Utilization of oil-based drilling cuttings pyrolysis residues of shale gas for the preparation of non-autoclaved aerated concrete. Constr Build Mater 162:359–368

Wang H et al (2019) Effect of water-soluble polymers on the performance of dust-suppression foams: Wettability, surface viscosity and stability. Colloids Surf, A 568:92–98

Wang Z et al (2023) The effect of interfacial tension on CO2 oil-based foam stability under different temperatures and pressures. Fuel 341:127755

Wu Y et al (2022) High-temperature CO2 for accelerating the carbonation of recycled concrete fines. J Build Eng 52:104526

Xiao J et al (2022) Influence of recycled powder derived from waste concrete on mechanical and thermal properties of foam concrete. J Build Eng 61:105203

Xu Y et al (2023) Effect of foam stabilization on the properties of foamed concrete modified by expanded polystyrene. J Build Eng 73:106822

Yadav S, Mehra A (2021) A review on ex situ mineral carbonation. Environ Sci Pollut Res 28(10):12202–12231

Yang S et al (2021) Preparation and properties of ready-to-use low-density foamed concrete derived from industrial solid wastes. Constr Build Mater 287:122946

Yekeen N et al (2017) Bulk and bubble-scale experimental studies of influence of nanoparticles on foam stability. Chin J Chem Eng 25(3):347–357

Yu W, Kanj MY (2022) Review of foam stability in porous media: the effect of coarsening. J Petrol Sci Eng 208:109698

Zhang H et al (2020) Properties of silt-based foamed concrete: a type of material for use in backfill behind an abutment. Constr Build Mater 261:119966

Zhang L et al (2022) Performance buildup of concrete cured under low-temperatures: use of a new nanocomposite accelerator and its application. Constr Build Mater 335:127529

Zhang H et al (2023a) Experimental study of moisture effects on spontaneous combustion of Baiyinhua lignite from individual particles to stockpile. Fuel 334:126774

Zhang H et al (2023b) Improving predictions of shale wettability using advanced machine learning techniques and nature-inspired methods: implications for carbon capture utilization and storage. Sci Total Environ 877:162944

Zhi K et al (2023) A review of CO2 utilization and emissions reduction: from the perspective of the chemical engineering. Process Saf Environ Prot 172:681–699